Gallium ion irradiation induced compaction and hardening of sputter deposited amorphous carbon thin films

Fritz Lehnert[a], Tilmann Häupl[b], Bernd Abel[a,b], S. G. Mayr[a,c]

[a] *Leibniz Institute for Surface Modification, Permoserstraße 15, 04318 Leipzig, Germany*
[b] *Wilhelm-Ostwald-Institute, Faculty of Chemistry and Mineralogy, University of Leipzig, Linnéstraße 3, 04103 Leipzig, Germany*
[c] *Division of Surface Physics, Faculty of Physics and Earth Sciences, University of Leipzig, Linnéstraße 5, 04103 Leipzig, Germany*

Abstract

We investigate sputter deposited amorphous carbon thin films modified by energetic 30 keV gallium ion irradiation. The samples are characterized combining atomic force microscopy and scanning electron microscopy with Raman spectroscopy measurements. Upon ion irradiation the development of a surface depression is observed, which saturates at a fluence of $10^{16}\,\mathrm{cm}^{-2}$. In this fluence range a transition in material behavior is observable with different analysis techniques. In addition, a surface smoothing and material hardening was measured. Stress relaxation as well as a transition from a sp^2-rich towards an sp^3-rich carbon hybridization are discussed as possible origin.

Keywords: ion irradiation, amorphous carbon, compaction, hardening

1. Introduction

Ion irradiation is a versatile tool for material modification and is widely used, e.g., within semiconductor industry, because it is able to modify the surface properties with nanometer precision [1]. Moreover, the modification of carbon is interesting as a plethora of applications has its origins in the carbon allotropy. For nanoporous or nanostructured carbon materials membrane and catalyst applications are reported [2–4]. In contrast, hard diamond or diamond like carbon coatings are utilized for wear resistance coatings or imprint lithography mold fabrication [5, 6]. Additionally, carbon is interesting for medical application, as it is non toxic and biocompatible [7, 8]. In contrast to purely scientific investigations of ion irradiation effects for MeV ions, ion energies of some keV are technologically highly relevant for surface and interface refining and modification processes [9–11].

Here, we investigated the impact of 30 keV gallium ion irradiation on sputter deposited amorphous carbon thin films, motivated by the potential applications. The effects are mapped and analyzed by atomic force microscopy (AFM), scanning electron microscopy (SEM), AFM-based mechanical property mapping as well as Raman spectroscopy. In our study we observe a strong material compaction, which is discussed with respect to different models: the forward sputtering mechanism and irradiation induced defect mediated stress relaxation.

2. Experimental

Carbon thin films were produced by sputter deposition at high vacuum conditions using wet oxidized silicon wafers with an oxide thickness larger than 700 nm as substrates. The base pressure of the system was 3×10^{-4} Pa or below and the system was flushed with high purity argon at a flow rate of 5 sccm for 5 min prior to sputter deposition. The carbon thin films were then deposited via argon plasma DC magnetron sputtering [12] at an average power of 100 W and an argon flow rate of 15 sccm. The sputtering time was chosen to result in films with a minimum thickness of 300 nm. The subsequent ion irradiation utilized a *Carl Zeiss Auriga* focused ion beam (FIB) using 30 keV gallium ions from an *Orsay Physics COBRA-FIB* column and fluences between 1×10^{14} cm^{-2} to 1×10^{18} cm^{-2} were used for ion irradiation of square areas with length of 10 µm. The samples were aligned for normal ion beam incidence to achieve maximum penetration depth. The ion beam scanned the sample line wise with a pixel dwell time of 0.1 µs and a resolution of 6144×4608 pixels, such that the total time of irradiation results in the desired irradiation fluence at the ion currents of 2 pA, 5 pA, 50 pA and 600 pA. The samples were analyzed by atomic force microscopy (AFM) with a *Bruker Icon Dimension*, by scanning electron microscopy (SEM) with a *Carl Zeiss Ultra 55* and by X-ray diffraction (XRD) measurements and x-ray reflectometry (XRR) using a *Rigaku Ultima IV* and a *Seifert XRD 3003 PTS*. Both instruments for XRD and XRR measurements use CuK_α radiation ($\lambda = 0.154\,18$ nm). The sample root mean square (RMS) roughness was determined from AFM images with analysis areas between 30 µm^2 to 90 µm^2. The area varied due to the exclusion of large contamination (e.g. dust particles). For Raman spectroscopy measurements an *Olympus IX71* microscope equipped with a *Verdi V5 coherent* frequency doubled Nd:YAG laser at 532 nm, a *HORIBA scientific iHR320* spectrometer and a *HORIBA scientific synapse* CCD camera were used. The laser output power

was set to 500 mW such that after the beam focusing and shaping setup containing optical filters, the sample was measured at ≈5 mW optical power [13]. With the laser wavelength and the numerical aperture of the objective lens $NA = 0.6$ the ideal laser focus diameter is estimated to 440 nm. The elastic properties were determined by AFM in *peak force quantitative nanomechanical mapping* (PFQNM) mode. That is, because the PFQNM mode of the AFM processes all data on the fly and the measurement software only implements the use for soft materials [1]. The program calculates the modulus using the DMT-model [14] given by the equation

$$F = k_c \delta_c = \frac{4}{3} \left(\frac{1 - {\nu_s}^2}{E_s} + \frac{1 - {\nu_c}^2}{E_c} \right)^{-1} \cdot \sqrt{R \cdot {\delta_s}^3} + F_{adh} \tag{1}$$

with the force F, the adhesion force F_{adh}, the cantilever spring constant k, the Poisson ratio ν, Young's modulus E, tip radius R, deformation δ and the indices c and s denoting the cantilever and sample respectively. However, the implementation for soft materials assumes $E_c \to \infty$, which does not hold for hard materials. Therefore, this was manually corrected for the measurements using a finite E_c for calculation of the modulus E_s. The measurement of hard materials requires stiff cantilevers, and thus uncoated silicon cantilevers of type *SD-T7L100SPL* from *NanoWorld AG* having an nominal stiffness of $k_c = 700\,\mathrm{N\,m^{-1}}$ were chosen. The tip was worn prior to measurement for at least 30 min to reduce tip wear effects during the measurement as demonstrated in previous contact resonance AFM studies [15, 16]. In order to determine the tip radius, a reference sample of Si(100) was measured and the equivalent tip radius was calculated to 99 nm. The elastic modulus of 170 GPa for Si(100) was used in all calculations [17]. The errors given for PFQNM measurements are full width at half maximum values of the modulus distribution function. From the physical perspective the measurement is limited by the probe's tip stiffness. For soft samples with $E_s \ll E_c$ the elastic modulus quantification is directly possible. The elastic modulus of stiffer samples ($E_s \approx E_c$) is usually underestimated and the error increases. For very stiff samples ($E_s \gg E_c$) careful consideration of the measurements is required, however, such stiff materials still yield high elastic moduli allowing for a qualitative assessment on comparative basis within the same

[1] While this is not a physical problem itself, it remains difficult in experiments as devices ship with proprietary software with limited configuration options.

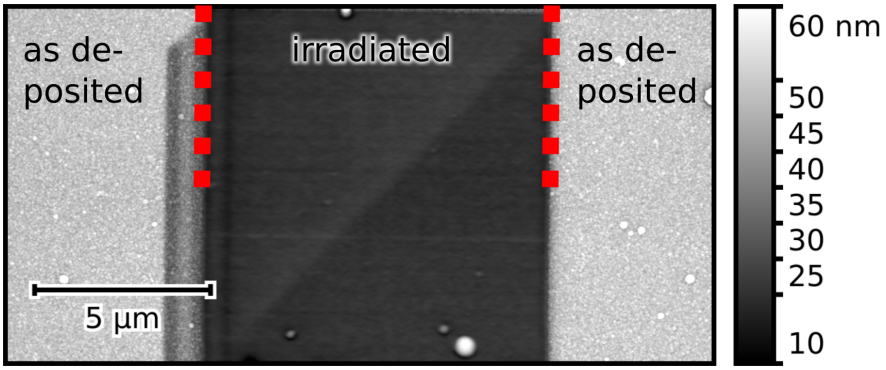

Figure 1: AFM measurement carbon irradiated at a fluence of $10^{17}\,\mathrm{cm}^{-2}$. The irradiated area is visible in the middle, surrounded by unirradiated material. For the irradiated area a depression is clearly visible and the smoothness can be observed.

measurement.

3. Results

The as-deposited carbon thin films exhibit a granular surface structure with typical lateral dimensions below 100 nm observed in SEM analysis and a surface roughness of 2.8 nm as determined by AFM measurements. A density of $1.6\,\mathrm{g\,cm}^{-3}$ for the as-deposited film was obtained by XRR measurement, which is low compared to other carbon materials, e.g., graphite with $2.3\,\mathrm{g\,cm}^{-3}$ or diamond with $3.5\,\mathrm{g\,cm}^{-3}$, but in good agreement with previous research [18]. The films showed no crystallinity in XRD measurements in the interesting range between 10° to 60° neither in an ordinary $2\theta/\theta$-measurement nor in a grazing incidence diffraction scan and are hence considered fully amorphous.

The fluence range for ion irradiation was chosen to be as large as possible. We found that no measurable material change was induced for fluences below $3 \times 10^{14}\,\mathrm{cm}^{-2}$. On the other hand, the film thickness limits the highest irradiation fluences. For fluences above $3 \times 10^{17}\,\mathrm{cm}^{-2}$ the film was completely sputtered off the silicon substrate. As a consequence the sample treatment and subsequent analysis was limited to the fluence range from $3 \times 10^{14}\,\mathrm{cm}^{-2}$ to $3 \times 10^{17}\,\mathrm{cm}^{-2}$.

3.1. Surface morphology measurements

After ion irradiation the carbon thin film surface topography was measured by AFM (Fig. 1) and the difference of surface height between irradiated and non-irradiated area is called *step height* hereafter and displayed in Fig. 2a. The step height was extracted from

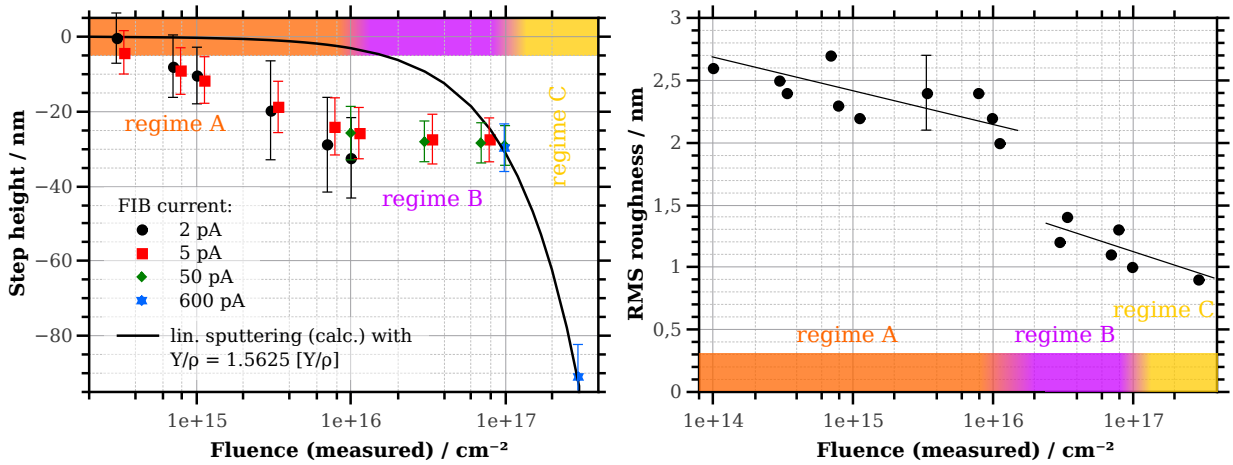

(a) AFM step height analysis. Measured data of a surface depression upon ion irradiation is depicted (full symbols) as well as a calculated sputtering behavior (solid line). For the measurements three regimes are visible, a logarithmic decrease for fluence below $1 \times 10^{16}\,\mathrm{cm}^{-2}$ (regime A), a plateau between $1 \times 10^{16}\,\mathrm{cm}^{-2}$ to $1 \times 10^{17}\,\mathrm{cm}^{-2}$ (regime B), and a linear decrease above $1 \times 10^{17}\,\mathrm{cm}^{-2}$ (regime C). A independence of FIB current is observed as irradiations with different currents align very well.

(b) Surface roughness as extracted from AFM measurement. A slight decrease in surface roughness occurs below $1 \times 10^{16}\,\mathrm{cm}^{-2}$, but the surface morphology stays unchanged as seen in SEM investigations. Exceeding $1 \times 10^{16}\,\mathrm{cm}^{-2}$ a significant drop of surface roughness is observable. The area in which roughness was evaluated was between $30\,\mu\mathrm{m}^2$ to $90\,\mu\mathrm{m}^2$ and the typical error is indicated for one measurement. The lines are guides to the eye.

Figure 2: AFM investigations of ion irradiated carbon.

AFM measurements by the evaluation of the height distribution function. It is clearly visible that a depression of the irradiated areas occurred for all fluences. Moreover the irradiations with different FIB currents align very well, showing that the process is current independent and no effect related to irradiation heating affects the process. Thus, different currents can be applied in order to reach irradiation fluences over three orders of magnitude. In addition to the measurement values (full symbols), a linear dependence as expected for sputtering is displayed (solid line). Comparing the measurements to the aforementioned linear dependence, we assign three different regions: A) a logarithmic decrease of step height below $10^{16}\,\mathrm{cm}^{-2}$, B) a saturation regime between $10^{16}\,\mathrm{cm}^{-2}$ to $10^{17}\,\mathrm{cm}^{-2}$, and C) a linear regime above $10^{17}\,\mathrm{cm}^{-2}$. In combination with the step height evolution we also consider the surface morphology development indicated by the surface' RMS roughness given in Fig. 2b. It is apparent that the surface roughness decreased abruptly on the transition from regime A to B with a decrease in RMS roughness by more than 0.5 nm. It is notable that this abrupt transition matches the transition between regime A and B of the step height measurements (Fig. 2a) and thus clearly indicates that some process affects the surface of the material

strongly reaching fluences of $\sim 10^{16}\,\mathrm{cm}^{-2}$.

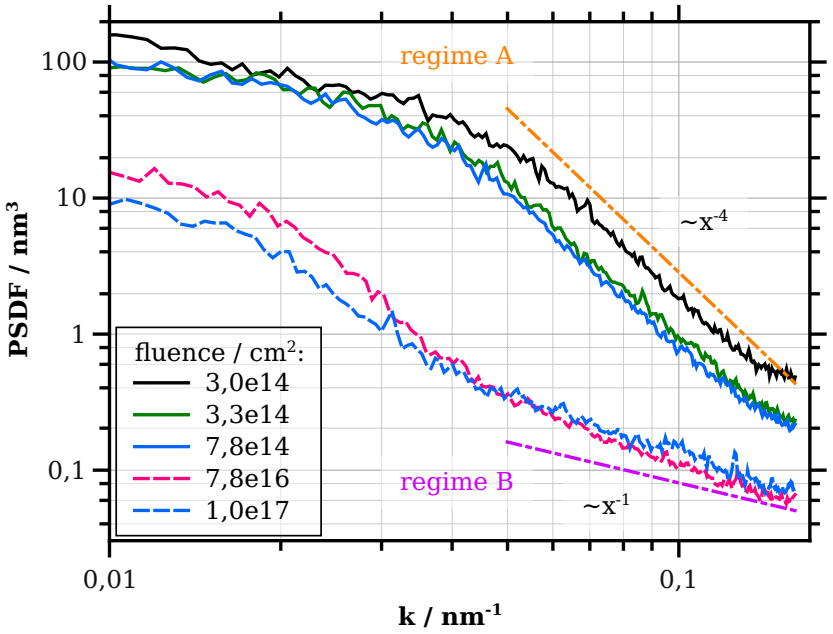

Figure 3: Power spectral density function (PSDF) of samples within regime A and B exemplary. For wavenumbers $k > 0.05\,\mathrm{nm}^{-1}$ samples from regime A show a dependence $\sim \frac{1}{k^4}$ and samples from regime B approximately a dependence $\sim \frac{1}{k}$.

The transition in surface morphology was also observed within an analysis of the power spectral density function (PSDF) between regime A and B. In general, the PSDF was always larger for samples of regime A compared to regime B (Fig. 3). More interesting, for wave numbers $k > 0.05\,\mathrm{nm}^{-1}$ the samples in regime A show a dependence $\sim \frac{1}{k^4}$, but the samples in regime B exhibit a dependence $\sim \frac{1}{k}$, that are commonly related to surface diffusion and plastic deformation, respectively [19].

3.2. Raman spectroscopy measurements

Our Raman spectroscopy investigations aim to detect changes of the bonding structure and especially the evolution of the sp^3 content of the material. Within various previous investigations on disordered carbon materials the G-peak wavenumber maximum ($\sim 1580\,\mathrm{cm}^{-1}$) is reliably correlated to different effects such as sp^3-to-sp^2-ratio or material stress [20, 21], such that we first analyze the G-peak wavenumber. The fluence dependent G-peak wavenumber, given in Fig. 4a, reveals different trends for the same regimes A and B discussed above and are thus in agreement with the AFM investigations. The G-peak frequency shifts to lower values from $1595\,\mathrm{cm}^{-1}$ to $1563\,\mathrm{cm}^{-1}$ with increasing fluence in regime A and then increases to $1586\,\mathrm{cm}^{-1}$ with increasing fluence in regime B.

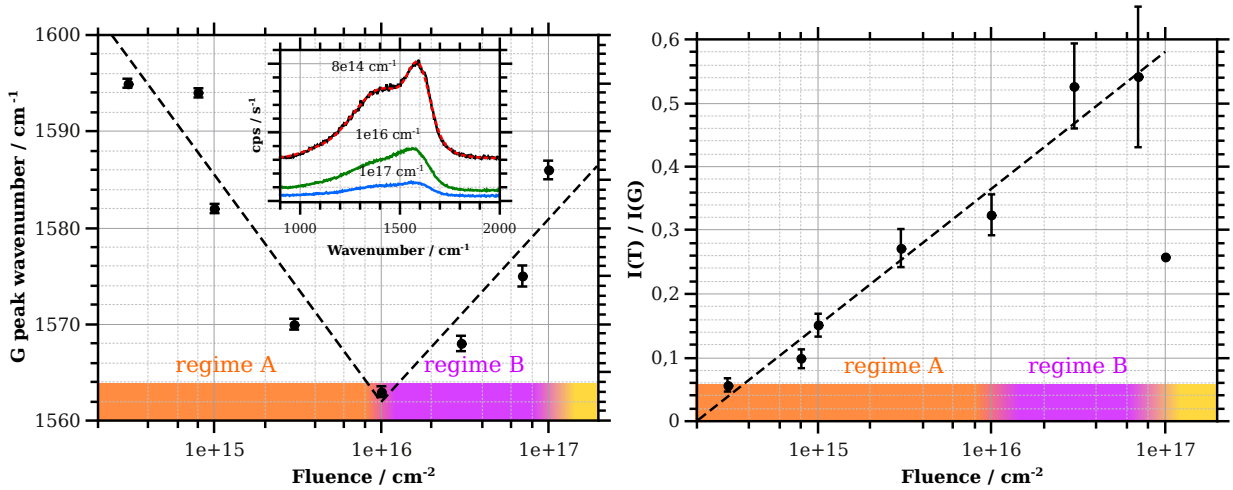

(a) G-peak maximum wavenumber in Raman spectroscopy measurements. A logarithmic decrease is visible below $10^{16}\,\mathrm{cm}^{-2}$ and an increase above that value. The *inset* shows measured Raman spectra for three fluences (solid) and a fit (dotted) exemplary.

(b) $\frac{I(T)}{I(G)}$ ratio for Raman spectroscopy measurements. A monotonic increase of $\frac{I(T)}{I(G)}$ ratio is visible for increasing fluence $<10^{17}\,\mathrm{cm}^{-2}$. The data point at $10^{17}\,\mathrm{cm}^{-2}$ is a measurement outlier.

Figure 4: Raman investigations of ion irradiated carbon. The lines are guides to the eye and the error bars indicate fit accuracy.

The D- and G-peak analysis resulted in a very good agreement for Raman lines between $1200\,\mathrm{cm}^{-1}$ to $2200\,\mathrm{cm}^{-1}$. However, a systematic deviation within all measurements was found between $900\,\mathrm{cm}^{-1}$ to $1200\,\mathrm{cm}^{-1}$, which was accounted for by an additional Gaussian peak centered at $1060\,\mathrm{cm}^{-1}$ close to the interval center, which we call T-peak (see discussion §4). Consequently, the intensity ratio $\frac{I(T)}{I(G)}$ can be calculated and is given in Fig. 4b. The $\frac{I(T)}{I(G)}$-ratio shows a monotonic increase from 0.06 to 0.54 with increasing fluence from $3 \times 10^{14}\,\mathrm{cm}^{-2}$ to $7 \times 10^{16}\,\mathrm{cm}^{-2}$ and does not show a transition at $10^{16}\,\mathrm{cm}^{-2}$. The outlier measurement value at $10^{17}\,\mathrm{cm}^{-1}$ can be explained by the decreased overall Raman signal intensity and hence increased analysis uncertainty with increasing irradiation fluence (see inset Fig. 4a) or by a slight laser misalignment during this measurement. As the signal intensity for the Raman peaks of carbon are too weak for proper evaluation above $10^{17}\,\mathrm{cm}^{-2}$, the measurements at these fluences were excluded from the evaluation.

3.3. Mechanical properties

Carbon is known as an element to show an extreme range of elastic moduli [22, 23] between 1076 GPa for diamond with $3.5\,\mathrm{g\,cm}^{-1}$ and 32 GPa for glassy carbon with densities below $2.0\,\mathrm{g\,cm}^{-1}$, depending on the bonding configuration. Therefore, elastic modulus measurements of the material were performed as complementary method to support the above

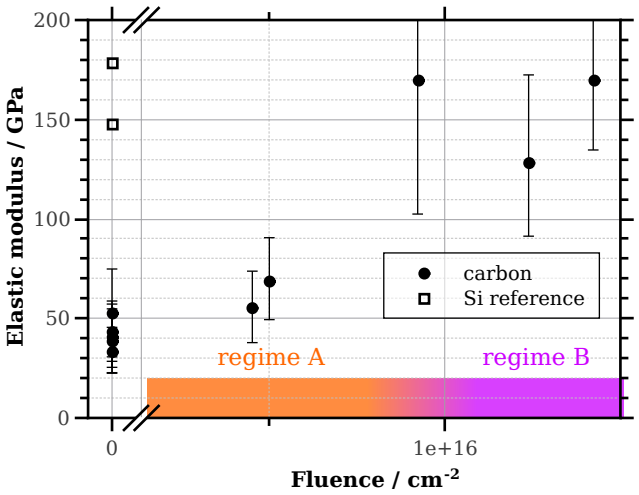

Figure 5: Measurement of the elastic modulus with PFQNM method at AFM. Next to the data for carbon (full circles) the measurements of the Si reference (open squares) are given. All irradiated samples show an increased modulus. While this increase is small, i.e., only about 45 %, for fluences of around $10^{15}\,\mathrm{cm}^{-2}$ in regime A, it is at least a factor of three for higher irradiation fluences in regime B.

findings of the Raman spectroscopy measurements and their interpretation.

The modulus measurements including the unirradiated reference samples and calibration measurements are shown in Fig. 5. Within the measurements one observes, that all irradiated samples show an increased modulus compared to the as-deposited films. The average modulus of the as-deposited films is 42 GPa which was consistently measured at different sample positions within the measurement error and compares to literature values of 32 GPa [22, 23]. For samples with irradiation fluences around $10^{15}\,\mathrm{cm}^{-2}$ (regime A) only a slight increase of the modulus of about 45 % was observed. In contrast, the modulus is increased by at least a factor of three for samples approaching and exceeding $10^{16}\,\mathrm{cm}^{-2}$ (regime B). The large errors for the high moduli are a result of the above discussed limitations of the technique, however, the modulus differences are large enough to be significant.

4. Discussion

4.1. Morphology

Starting with the discussion of regime A, the observed surface depression (Fig. 2a) is attributed to a material compaction. Material compaction upon ion irradiation was reported before for low density phases of various material systems, such as silica [24, 25]. With the observation of a low density for our as-deposited film of only $1.6\,\mathrm{g\,cm}^{-3}$, we conclude that material compaction is plausible when expecting an ion beam induced relaxation towards a

denser and more stable material configuration. The low density of our as-deposited films originates from the synthesis method, i.e., sputtering deposition at low temperatures. In accordance with the structure zone model [26] the films grow in amorphous porous network structures containing voids.

Ion irradiation of the material causes displacements and disorder to be introduced, which drives it out of equilibrium and, at the same time, energy is deposited enhancing processes like diffusion [27] or viscous flow [28, 29] enabling a more rapid relaxation towards an equilibrium. The energy deposition in the material by the primary ion is mainly caused by nuclear stopping ($\varepsilon_n = 1.42\,\mathrm{keV\,nm^{-1}}$). And as the electronic stopping is small ($\varepsilon_e = 0.22\,\mathrm{keV\,nm^{-1}}$) at the given ion energy [30], we only discuss mechanisms relying on the nuclear displacements. The material modification with ions may be regarded as a complex interplay of different driving and relaxation mechanisms of which forward sputtering, capillarity and internal stresses, as well as viscous flow and diffusion are discussed below.

The atomic peening or forward sputtering model [31] describes atomic displacements with a preferential displacement vector in direction of the primary ion, such that the atoms will be incorporated in the underlying material layers and consequently increase the average material density in this layer. Forward sputtering therefore promotes a material transport towards deeper material layers and densifies these layers. With the synonymous name atomic peening the process is often applied to surface atoms, as it is expected that the forward sputtering is the most likely in the near surface layer of the material, where the primary ion still possesses the major part of its momentum in the direction of the incident ion beam. When atomic peening is taking place at the surface, a severe change of surface morphology may also be observed. Within our experiments the surface morphology only changes slightly within regime A. However, the peening process can also occur within the bulk material, making effects on the surface small. While the classical sputtering process or atomic displacement events follow a linear dependence on fluence, such dependence only holds as long as successive events are independent, i.e., the material has no memory of the previous events. This is not the case for bulk irradiation, where damage remains in the material and adds up with subsequent events. In such a case, a damage accumulation up to a maximum total damage occurs, so that the damage rate decays and a logarithmic decrease can be expected, when plausibly assuming a random process for ion irradiation.

Growing films at low temperatures yields low thermal stresses, but intrinsic stresses of tensile nature are expected to be large [31]. Average tensile stresses of 3 GPa have been reported for amorphous carbon films, but the stress distribution is expected to be non homogeneous with local compressive and tensile stresses up to ∼40 GPa [32]. Additionally, small voids ($r < 5\,\mathrm{nm}$) may be present in the as-deposited layer, for which capillarity induced by the surface tension results in a (negative) pressure. The pressure Δp due to the surface curvature R can be estimated with the *Young-Laplace-equation*[2] for a spherical object reading $\Delta p = \frac{2\gamma}{R}$ with the surface tension γ. While the surface tension is different from the surface free energy [33], the surface tension is generally difficult to measure. Thus, the surface free energy will be used as an estimate, motivated by the fact that we consider a case where plastic deformation is probable. The surface free energy for amorphous carbon films was reported in the range of $33\,\mathrm{mN\,m^{-1}}$ to $56\,\mathrm{mN\,m^{-1}}$ with commonly given average of $\sim 40\,\mathrm{mN\,m^{-1}}$ [34–36]. A pressure due to capillarity of −80 MPa is then calculated assuming a pore radius of 1 nm. Nevertheless, does this effect contribute to a overall tensile stress in the material. When a stress relaxation is now induced, the material will relax into a denser state, leading to a volume decrease and material compaction.

Macroscopically, irradiation induced diffusion [27] and irradiation induced viscous flow [28, 29] contribute to stress relaxation. Microscopically, both mechanisms rely on defect creation and migration within the material. Therefore, the two macroscopic effects might not be discerned on the atomistic scale and are discussed in view of defect generation and migration as follows. For a defect generated in amorphous covalent materials due to the displacement of an atom by the ion irradiation, it was shown that the interstitial relaxes into the amorphous matrix rapidly, while the vacancy has a longer life time [37, 38]. Additionally, severe stress relaxation upon defect generation is known to occur for metal and semiconductor thin films upon ion irradiation [29, 38]. On an atomistic scale, the interstitials create a local compressive stress field which counteracts the tensile stresses in the matrix and, more importantly, induces stress relaxation by atomic rearrangements. As a consequence, the vacancies also mainly contribute to the stress relaxation, as they, e.g., mediate the viscous flow as effectively as interstitials [28]. Comparing our AFM measurements to previous studies of the stress relaxation in thin metal films [29], we find a quite similar behavior with a strong

[2] sometimes also called *Gibbs-Thomson-equation*

logarithmic decrease for the start of the irradiation, which saturates at some fluence, when all stresses are relaxed, i.e., at a fluence of $10^{16}\,\mathrm{cm}^{-2}$ in our case.

Relaxation processes driven by the irradiation induced defects will be the most pronounced slightly below[3] the projected range of 32.2 nm for 30 keV gallium in $1.6\,\mathrm{g\,cm}^{-3}$ carbon, as calculated by SRIM [30]. Starting at around 32 nm depth a compacted material layer will build up. In consequence the increased material density leads to a reduced projected range, e.g., only 15.5 nm in $3.5\,\mathrm{g\,cm}^{-3}$ carbon. With the shift in projected range a new formerly less modified layer closer to the sample surface is now being altered and the compacted region will gradually expand towards the sample surface. Eventually, the compacted material reaches the sample surface at $10^{16}\,\mathrm{cm}^{-2}$ and the samples surface morphology changes significantly in regime B indicated by an abrupt surface roughness decrease (see Fig. 2b). The surface morphology is then no longer given by the as-deposited porous structure, instead, it is determined by the compacted material phase, showing a very smooth surface with a root mean square (RMS) roughness between 1.4 nm to 0.9 nm. At the same time the transition of the PSDF from a $\sim \frac{1}{k^4}$ to a $\sim \frac{1}{k}$ dependence indicates a transition of the strongest surface relaxation mechanism from surface diffusion to viscous flow [39]. Moreover, no further material relaxation will be induced upon ongoing irradiation, as all material reached by the ion beam is already modified, so that the formation of a depression will stop in regime B.

Within regime B a condition is reached were the surface remains unchanged, which is surprising, because sputtering is expected to become significant for increasing fluence, i.e., the expected sputtering is calculated [30] to contribute to the depression with 6 nm or more for a fluence of $10^{17}\,\mathrm{cm}^{-2}$ while contributing only with 0.6 nm at a fluence of $10^{16}\,\mathrm{cm}^{-2}$. With the experimentally observed stagnation of step height decrease in this regime we can also exclude a non-linear sputter yield increase due to gallium incorporation or morphology change for the depression forming in regime A, as such an effect should prevail or increase for increasing fluence, making a stagnation of the step height decrease implausible. In any case, the sputtering yield was reported to decrease for the addition of big surfactant atoms on silicon [40]. Furthermore, even assuming a fluence dependent sputtering with linear dependence of sputter yield on fluence [41], would only yield a quadratic decrease of step height with fluence and cannot describe the observed logarithmic behavior in regime A. Therefore, we conclude

[3] More precise at the maximum of the vacancy distribution.

that an increased non-linear sputtering can be neglected when considering the depression development within regime A.

The stabilization of the step height plateau in regime B is probably the most elusive feature of the observed behavior for the ion irradiation of the carbon thin film. The aforementioned processes were discussed to lead to a step height decrease upon increased irradiation fluence, which is certainly true for material sputtering at all fluences. However, the introduction of defects in the material is more subtle and causes different processes. While it has been discussed before that the generated defects allow relaxation of intrinsic stresses at low fluences, generated defects also introduce stresses in the material themselves. Therefore, after stress relaxation by the initial irradiation (at $10^{16}\,\mathrm{cm}^{-2}$), a continued irradiation will build up new stresses because the interstitials in particular introduce a high excess volume. The introduction of excess volume, however, leads to a material swelling and thus to a step height increase, which can be observed for, e.g., diamond material [42, 43]. This process is often discussed within the framework of nanoporous structure generation in amorphous materials under heavy ion irradiation ([38], and references therein) and is thus not described here in detail. Still, it remains to be pointed out that the defect induced swelling process has a condition specific threshold and saturation fluence and is thus only operational within a certain fluence regime. From our measurements we conclude that this regime is between $\sim 10^{16}\,\mathrm{cm}^{-2}$ to $\sim 10^{17}\,\mathrm{cm}^{-2}$ for our system and the swelling behavior therefore counteracts the depression formation via the sputtering process within regime B leading to the plateau observed.

Finally, when the above discussed defect induced material changes all reached a steady state condition, the material sputtering is the dominating effect, as seen within regime C until the entire carbon thin film is removed.

4.2. Raman spectroscopy measurements

The material compaction and stress relaxation is likely linked to a significant change in bonding structure from a sp^2-network towards a sp^3-rich material which, in turn, exhibits properties like high density and stiffness, commonly seen for diamond like carbon [44, 45]. As various previous investigations on disordered carbon materials correlate the G-peak wavenumber maximum ($\sim 1580\,\mathrm{cm}^{-1}$) to different effects such as sp^3-to-sp^2-ratio or material stress [20, 21], we first focus on the discussion of G-peak wavenumber shift.

The decrease of G-peak wavenumber in regime A (Fig. 4a) is attributed to the above

described ion irradiation induced stress relaxation. Raman G-peak shifts were reported previously for stressed materials to be of the same magnitude, with the stressed states exhibiting the higher wavenumbers [46, 47]. Within these investigations compressive stresses were studied, however, a tensile stress is expected to cause a wavenumber increase, too. This can be explained in view of the phonons acting close to the minimum of the Lennard-Jones potential as a model system for atomic interaction potentials. Therefore, film stresses, both compressive and tensile, lead to an increased effective spring constant and thus to an increased frequency for phonon vibrations, as they move the equilibrium position out of the minimum of the potential. The G-peak wavenumber shift happens on a logarithmic scale, which is in agreement with the AFM measurements, when considering that the G-peak shift correlates linearly with the material stress [47]. The shift to higher values within regime B can be understood in two ways. On the one hand, it can be induced by increased compressive stresses as discussed above. On the other hand, a shift to higher values was also reported for the transition from amorphous carbon (a-C) to tetrahedral amorphous carbon (ta-C), which is accompanied by a large increase of sp^3 content [48]. At closer inspection, both descriptions can be seen as equivalent, as the transition from a-C to ta-C is accompanied by the occurrence of compressive stresses [49]. For these reasons, the shift to higher values of G-peak wavenumber within regime B indicates a material transition towards a sp^3-rich material.

A T-peak originating from sp^3-bond vibrations was reported in ta-C for the very wavenumber of $1060\,\mathrm{cm}^{-1}$, and the $\frac{I(T)}{I(G)}$-ratio was correlated to the sp^3 content of the material [45]. Hence, our peak at $1060\,\mathrm{cm}^{-1}$ was identified as T-peak contribution and the $\frac{I(T)}{I(G)}$-ratio given in Fig. 4b can be utilized as a measure of the sp^3-content. The monotonic increase of $\frac{I(T)}{I(G)}$-ratio implies an increased sp^3 ratio with increased irradiation fluence. Assuming applicability of the correlation between $\frac{I(T)}{I(G)}$-ratio and sp^3 fraction given by Ferrari and Robertson [21], the sp^3 ratio in our samples can be estimated to increase from below 20 % to over 80 %. Considering the synthesis of our samples and assuming a monotonic relation for the correlation between $\frac{I(T)}{I(G)}$-ratio and sp^3 fraction also outside the regime studied by Ferrari and Robertson, we estimate that the sp^3 fraction of the as-deposited samples is insignificantly small, but is reaching 60 % when approaching a fluence of $\sim 10^{16}\,\mathrm{cm}^{-1}$ and further increases up to $\approx$85 % at higher fluences.

4.3. Mechanical properties

A material compaction and increased sp^3-content leads to an increased material stiffness, as seen for ta-C [44], such that the measurements of the mechanical properties can be seen as complementary to the Raman spectroscopy investigations. The significantly increased elastic modulus induced by ion irradiation (Fig. 5) is therefore in good agreement with the results of the AFM and Raman spectroscopy measurements and confirms the presence of a compacted and strongly sp^3-bonded carbon surface layer. The increase is especially pronounced above fluences of $\sim 10^{16}\,\mathrm{cm}^{-2}$ where a notable contribution ($\geq$60 %) of the sp^3-content exists and the material is compressively stressed, according to our aforementioned Raman spectroscopy investigations.

5. Conclusions

Summarizing our results for the 30 keV gallium ion irradiation of the amorphous carbon thin films, we observe a pronounced material compaction together with a surface smoothing and material hardening. A transition in material behavior occurs at a fluence of $10^{16}\,\mathrm{cm}^{-2}$, seen consistently with different, complementary analysis techniques. Our AFM and Raman spectroscopy measurements can be interpreted as a material compaction and relaxation of tensile stress below $10^{16}\,\mathrm{cm}^{-2}$, as well as a compressive stress generation accompanied by a transition from a mainly sp^2-hybridized network towards a sp^3-rich material above $10^{16}\,\mathrm{cm}^{-2}$. In agreement with the increasing sp^3-content and compressive stress, a significant material hardening, resulting in films with an elastic modulus comparable to Si(100) or exceeding it, was found above $10^{16}\,\mathrm{cm}^{-2}$. A material swelling as a relaxation process for compressive stress, counteracts the expected material sputtering within the fluence regime of $10^{16}\,\mathrm{cm}^{-2}$ to $10^{17}\,\mathrm{cm}^{-2}$.

Different processes were discussed to be responsible for the material behavior, including atomic peening and the defect driven relaxation of intrinsic stresses originating from film growth. Furthermore, our surface morphology analysis suggests surface diffusion and viscous flow, to be primary surface relaxation mechanisms within the different regimes. From our experiments we therefore conclude that the ion irradiation induced defect generation, annihilation and migration are key processes for the material behavior under ion irradiation.

6. Acknowledgements

Funding by the *German Science Foundation* (DFG) - Project PARTACT is gratefully acknowledged. This research was performed within the Leipzig Graduate School of Natural Sciences, *Building with Molecules and Nanoscale objects* (BuildMoNa) that was established within the German Excellence Initiative also by the DFG. Further, we thank Dr. Carsten Bundesmann for discussion on Raman spectroscopy measurements.

References

[1] L. N. Large, R. W. Bicknell, Ion-implantation doping of semiconductors, J. Mater. Sci. 2 (1967) 589–609.

[2] A. F. Collings, F. Caruso, Biosensors: recent advances, Reports Prog. Phys. 60 (1997) 1397–1445.

[3] G. Q. Lu, X. S. Zhao (Eds.), Nanoporous Materials: Science and Engineering, Series on Chemical Engineering, Imperial College Press, London, 2004. URL: http://ebooks.worldscinet.com/ISBN/9781860946561/9781860946561.html. doi:10.1142/9781860946561.

[4] J. Tang, J. Liu, N. L. Torad, T. Kimura, Y. Yamauchi, Tailored design of functional nanoporous carbon materials toward fuel cell applications, Nano Today 9 (2014) 305–323.

[5] A. Voevodin, J. Zabinski, Supertough wear-resistant coatings with 'chameleon' surface adaptation, Thin Solid Films 370 (2000) 223–231.

[6] Š. Meškinis, V. Kopustinskas, K. Šlapikas, S. Tamulevičius, A. Guobienë, R. Gudaitis, V. Grigaliunas, Ion beam synthesis of the diamond like carbon films for nanoimprint lithography applications, Thin Solid Films 515 (2006) 636–639.

[7] R. J. Narayan, R. Aggarwal, W. Wei, C. Jin, N. A. Monteiro-Riviere, R. Crombez, W. Shen, Mechanical and biological properties of nanoporous carbon membranes., Biomed. Mater. 3 (2008) 034107.

[8] N. L. Torad, Y. Li, S. Ishihara, K. Ariga, Y. Kamachi, H.-Y. Lian, H. Hamoudi, Y. Sakka, W. Chaikittisilp, K. C.-W. Wu, Y. Yamauchi, MOF-derived Nanoporous Carbon as Intracellular Drug Delivery Carriers, Chem. Lett. 43 (2014) 717–719.

[9] A. A. Tseng, Recent developments in micromilling using focused ion beam technology, J. Micromechanics Microengineering 14 (2004) R15–R34.

[10] C. A. Volkert, A. M. Minor, Focused Ion Beam Microscopy and Micromachining, MRS Bull. 32 (2007) 389–399.

[11] L. Bischoff, Application of mass-separated focused ion beams in nano-technology, Nucl. Instruments Methods Phys. Res. Sect. B 266 (2008) 1846–1851.

[12] G. Bräuer, B. Szyszka, M. Vergöhl, R. Bandorf, Magnetron sputtering – Milestones of 30 years, Vacuum 84 (2010) 1354–1359.

[13] R. Flyunt, W. Knolle, A. Kahnt, C. E. Halbig, A. Lotnyk, T. Häupl, A. Prager, S. Eigler, B. Abel, High quality reduced graphene oxide flakes by fast kinetically controlled and clean indirect UV-induced radical reduction, Nanoscale 8 (2016) 7572–7579.

[14] B. Derjaguin, V. Muller, Y. Toporov, Effect of contact deformations on the adhesion of particles, J. Colloid Interface Sci. 53 (1975) 314–326.

[15] A. M. Jakob, M. Müller, B. Rauschenbach, S. G. Mayr, Nanoscale mechanical surface properties of single crystalline martensitic Ni–Mn–Ga ferromagnetic shape memory alloys, New J. Phys. 14 (2012) 033029.

[16] A. M. Jakob, J. Buchwald, B. Rauschenbach, S. G. Mayr, Nanoscale-resolved elasticity: contact mechanics for quantitative contact resonance atomic force microscopy, Nanoscale 6 (2014) 6898–6910.

[17] M. A. Hopcroft, W. D. Nix, T. W. Kenny, What is the Young's Modulus of Silicon?, J. Microelectromechanical Syst. 19 (2010) 229–238.

[18] D. W. M. Lau, a. Moafi, M. B. Taylor, J. G. Partridge, D. G. McCulloch, R. C. Powles, D. R. McKenzie, The structural phases of non-crystalline carbon prepared by physical vapour deposition, Carbon N. Y. 47 (2009) 3263–3270.

[19] W. W. Mullins, Theory of Thermal Grooving, J. Appl. Phys. 28 (1957) 333.

[20] J. Schwan, S. Ulrich, V. Batori, H. Ehrhardt, S. R. P. Silva, Raman spectroscopy on amorphous carbon films, J. Appl. Phys. 80 (1996) 440–447.

[21] A. C. Ferrari, J. Robertson, Raman spectroscopy of amorphous, nanostructured, diamond-like carbon, and nanodiamond, Philos. Trans. R. Soc. A Math. Phys. Eng. Sci. 362 (2004) 2477–2512.

[22] H. J. McSkimin, W. L. Bond, Elastic Moduli of Diamond, Phys. Rev. 105 (1957) 116–121.

[23] J. Robertson, Mechanical properties and coordinations of amorphous carbons, Phys. Rev. Lett. 68 (1992) 220–223.

[24] S. Klaumünzer, L. Changlin, S. Löffler, M. Rammensee, G. Schumacher, Plastic flow of vitreous silica and Pyrex during bombardment with fast heavy ions, Nucl. Instruments Methods Phys. Res. Sect. B 39 (1989) 665–669.

[25] W. Wagner, F. Rauch, R. Feile, C. Ottermann, K. Bange, Compaction of tungsten oxide films by ion-beam irradiation, Thin Solid Films 235 (1993) 228–233.

[26] J. A. Thornton, High Rate Thick Film Growth, Annu. Rev. Mater. Sci. 7 (1977) 239–260.

[27] G. J. Dienes, A. C. Damask, Radiation Enhanced Diffusion in Solids, J. Appl. Phys. 29 (1958) 1713–1721.

[28] S. G. Mayr, Y. Ashkenazy, K. Albe, R. Averback, Mechanisms of Radiation-Induced Viscous Flow: Role of Point Defects, Phys. Rev. Lett. 90 (2003) 055505.

[29] S. G. Mayr, R. Averback, Effect of ion bombardment on stress in thin metal films, Phys. Rev. B 68 (2003) 214105.

[30] J. F. Ziegler, M. Ziegler, J. P. Biersack, SRIM – The stopping and range of ions in matter (2010), Nucl. Instruments Methods Phys. Res. Sect. B 268 (2010) 1818–1823.

[31] J. A. Thornton, D. W. Hoffman, Stress-related effects in thin films, Thin Solid Films 171 (1989) 5–31.

[32] P. C. Kelires, Elastic Properties of Amorphous Carbon Networks, Phys. Rev. Lett. 73 (1994) 2460–2463.

[33] R. Shuttleworth, The Surface Tension of Solids, Proc. Phys. Soc. Sect. A 63 (1950) 444–457.

[34] J. S. Chen, S. P. Lau, B. K. Tay, G. Y. Chen, Z. Sun, Y. Y. Tan, G. Tan, J. W. Chai, Surface energy of amorphous carbon films containing iron, J. Appl. Phys. 89 (2001) 7814–7819.

[35] M. Stüber, L. Niederberger, F. Danneil, H. Leiste, S. Ulrich, A. Welle, M. Marin, H. Fischer, Surface Topography, Surface Energy and Wettability of Magnetron-Sputtered Amorphous Carbon (a-C) Films and Their Relevance for Platelet Adhesion, Adv. Eng. Mater. 9 (2007) 1114–1122.

[36] A. Zebda, H. Sabbah, S. Ababou-Girard, F. Solal, C. Godet, Surface energy and hybridization studies of amorphous carbon surfaces, Appl. Surf. Sci. 254 (2008) 4980–4991.

[37] T. K. Chaki, J. C. M. Li, Radiation damage in an amorphous lennard-jones solid a computer simulation, Philos. Mag. Part B 51 (1985) 557–565.

[38] S. G. Mayr, R. Averback, Ion-irradiation-induced stresses and swelling in amorphous Ge thin films, Phys. Rev. B 71 (2005) 134102.

[39] W. W. Mullins, Flattening of a nearly plane solid surface due to capillarity, J. Appl. Phys. 30 (1959) 77–83.

[40] H. Hofsäss, K. Zhang, Surfactant sputtering, Appl. Phys. A 92 (2008) 517–524.

[41] P. Blank, K. Wittmaack, Energy and fluence dependence of the sputtering yield of silicon bombarded with argon and xenon, J. Appl. Phys. 50 (1979) 1519–1528.

[42] E. W. Maby, Volume expansion of ion-implanted diamond, Appl. Phys. Lett. 39 (1981) 157–158.

[43] J. Prins, T. Derry, J. Sellschop, Volume expansion of diamond during ion implantation, Phys. Rev. B 34 (1986) 8870–8874.

[44] H.-J. Scheibe, B. Schultrich, H. Ziegele, P. Siemroth, Deposition of superhard amorphous carbon films by pulsed arc sources, IEEE Trans. Plasma Sci. 25 (1997) 685–688.

[45] A. C. Ferrari, J. Robertson, M. G. Beghi, C. E. Bottani, R. Ferulano, R. Pastorelli, Elastic constants of tetrahedral amorphous carbon films by surface Brillouin scattering, Appl. Phys. Lett. 75 (1999) 1893–1895.

[46] J. W. Ager, S. Anders, A. Anders, I. G. Brown, Effect of intrinsic growth stress on the Raman spectra of vacuum-arc-deposited amorphous carbon films, Appl. Phys. Lett. 66 (1995) 3444–3446.

[47] J.-K. Shin, C. S. Lee, K.-R. Lee, K. Y. Eun, Effect of residual stress on the Raman-spectrum analysis of tetrahedral amorphous carbon films, Appl. Phys. Lett. 78 (2001) 631–633.

[48] A. C. Ferrari, B. Kleinsorge, N. A. Morrison, A. Hart, V. Stolojan, J. Robertson, Stress reduction and bond stability during thermal annealing of tetrahedral amorphous carbon, J. Appl. Phys. 85 (1999) 7191–7197.

[49] P. J. Fallon, V. S. Veerasamy, C. A. Davis, J. Robertson, G. A. J. Amaratunga, W. I. Milne, J. Koskinen, Properties of filtered-ion-beam-deposited diamondlike carbon as a function of ion energy, Phys. Rev. B 48 (1993) 4777–4782.